JCI The Journal of Clinical Investigation

Adverse outcomes in SARS-CoV-2–infected pregnant mice are gestational age–dependent and resolve with antiviral treatment

Patrick S. Creisher, … , Andrew Pekosz, Sabra L. Klein

J Clin Invest. 2023;133(20):e170687. https://doi.org/10.1172/JCI170687.

Research Article | Reproductive biology | Therapeutics

Graphical abstract

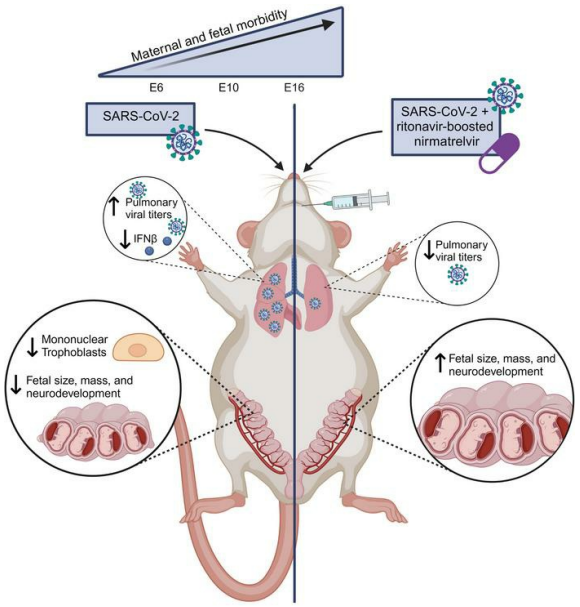

Adverse outcomes in SARS-CoV-2–infected pregnant mice are gestational age–dependent and resolve with antiviral treatment

Patrick S. Creisher,[1] Jamie L. Perry,[1] Weizhi Zhong,[1] Jun Lei,[2] Kathleen R. Mulka,[3] W. Hurley Ryan III,[4] Ruifeng Zhou,[1] Elgin H. Akin,[1] Anguo Liu,[3] Wayne Mitzner,[4] Irina Burd,[2] Andrew Pekosz,[1,4] and Sabra L. Klein[1]

[1]W. Harry Feinstone Department of Molecular Microbiology and Immunology, The Johns Hopkins Bloomberg School of Public Health, Baltimore, Maryland, USA [2]Department of Obstetrics, Gynecology & Reproductive Sciences, University of Maryland School of Medicine, Baltimore, Maryland, USA [3]Department of Molecular and Comparative Pathobiology, The Johns Hopkins School of Medicine, Baltimore, Maryland, USA. [4]Department of Environmental Health and Engineering, The Johns Hopkins Bloomberg School of Public Health, Baltimore, Maryland, USA.

SARS-CoV-2 infection during pregnancy is associated with severe COVID-19 and adverse fetal outcomes, but the underlying mechanisms remain poorly understood. Moreover, clinical studies assessing therapeutics against SARS-CoV-2 in pregnancy are limited. To address these gaps, we developed a mouse model of SARS-CoV-2 infection during pregnancy. Outbred CD1 mice were infected at E6, E10, or E16 with a mouse-adapted SARS-CoV-2 (maSCV2) virus. Outcomes were gestational age–dependent, with greater morbidity, reduced antiviral immunity, greater viral titers, and impaired fetal growth and neurodevelopment occurring with infection at E16 (third trimester equivalent) than with infection at either E6 (first trimester equivalent) or E10 (second trimester equivalent). To assess the efficacy of ritonavir-boosted nirmatrelvir, which is recommended for individuals who are pregnant with COVID-19, we treated E16-infected dams with mouse-equivalent doses of nirmatrelvir and ritonavir. Treatment reduced pulmonary viral titers, decreased maternal morbidity, and prevented offspring growth restriction and neurodevelopmental impairments. Our results highlight that severe COVID-19 during pregnancy and fetal growth restriction is associated with heightened virus replication in maternal lungs. Ritonavir-boosted nirmatrelvir mitigated maternal morbidity along with fetal growth and neurodevelopment restriction after SARS-CoV-2 infection. These findings prompt the need for further consideration of pregnancy in preclinical and clinical studies of therapeutics against viral infections.

Introduction

Pregnancy is a risk factor for developing severe COVID-19, with individuals who are pregnant at increased risk of hospitalization, mechanical ventilation, and mortality compared with patients who are not pregnant (1–9). The time of infection during gestation contributes to increased severity, with hospitalization and intensive care unit admission being greater in the third than either the second or first trimester (10, 11). While the specific mechanisms that contribute to the increased risk of severe outcomes during pregnancy are not specified, both immunological and physiological changes are likely involved. The immune system undergoes unique shifts as pregnancy progresses, including increased regulatory T and B lymphocytes as well as reduced cytotoxic and cellular immunity, to protect the developing semiallogenic fetus (12, 13). The general antiinflammatory shift during the second and third trimesters also may increase the risk of severe outcomes from viruses, including SARS-CoV-2, by blunting antiviral immune responses (13). Moreover, physiological changes associated with pregnancy, including cardiovascular, respiratory, endocrine, and metabolic alterations may further contribute to disease severity (14). While these pregnancy-associated factors are hypothesized to contribute to severe disease and death following infection with SARS-CoV-2, the exact mechanisms contributing to severe COVID-19 disease during pregnancy in humans are unknown.

In addition to causing severe outcomes in individuals who are pregnant, SARS-CoV-2 infection during pregnancy also can result in adverse fetal outcomes, including preterm birth, stillbirth, small size for gestational age, and reduced birth weight (5, 15–19), as well as increased risks of neurobehavioral deficits and delayed motor skills in infants born to infected mothers (20, 21). Like maternal disease, adverse perinatal and fetal outcomes appear to be influenced by gestational age, with greater risk observed after infection in the third than either the second or first trimesters (10, 20, 22). Direct placental infection or vertical transmission of SARS-CoV-2 is exceedingly rare (23–25), and thus is unlikely to be the source of adverse fetal and neonatal outcomes. The exact mechanisms underlying these adverse outcomes remain unknown.

Because of their risk for severe COVID-19 and adverse pregnancy outcomes, individuals who are pregnant are prioritized for receipt of available emergency-use authorized antivirals and vac-

Authorship note: PSC and JLP are co–first authors.
Conflict of interest: The authors have declared that no conflict of interest exists.

Submitted: March 21, 2023; **Accepted:** August 10, 2023; **Published:** October 16, 2023.
Reference information: *J Clin Invest*. 2023;133(20):e170687.
https://doi.org/10.1172/JCI170687.

cines (26–28), despite being excluded from clinical trials of SARS-CoV-2 vaccines and antivirals (29). SARS-CoV-2 mRNA vaccines have been proven to be safe and effective during pregnancy (30–32), and the United States Centers for Disease Control and Prevention recommends vaccination for people who are pregnant, recently pregnant, or trying to become pregnant (30). The safety and efficacy of SARS-CoV-2 antivirals during pregnancy has not been as well studied. In the United States, people who are pregnant are recommended to receive the antivirals remdesivir (brand name Veklury) and ritonavir-boosted nirmatrelvir (brand name Paxlovid) when indicated (33). While neither antiviral included individuals who were pregnant in their clinical trials (34), observational studies of remdesivir indicate its safety and efficacy in pregnant populations (35). Nirmatrelvir is an oral antiviral that inhibits the SARS-CoV-2 M^{PRO} protease and is packaged with ritonavir, a previously established HIV protease inhibitor and pharmacologic booster, which does not have direct antiviral effects on SARS-CoV-2 but instead works to prolong the bioavailability of nirmatrelvir through the inhibition of the hepatic cytochrome P-450 (CYP) 3A4 enzyme (36, 37). Ritonavir-boosted nirmatrelvir treatment during pregnancy appears safe, with no adverse obstetric outcomes reported in small observational studies (38–40). The efficacy of ritonavir-boosted nirmatrelvir in preventing SARS-CoV-2 infection or disease during pregnancy remains an open question, in part because most studies to date were not designed to evaluate efficacy (38–40).

Animal models of microbial infections during pregnancy provide mechanistic insight into adverse maternal and fetal outcomes by enabling deeper analysis of vertical transmission and maternal and fetal immune responses. Animal models have elucidated the pathogenesis of infections such Zika virus, influenza A virus, *Plasmodium falciparum*, and Group B *Streptococcus* infections during pregnancy (26). In the absence of human clinical trials, animal models of infection during pregnancy can be used to characterize the safety and efficacy of therapeutics in this high-risk population. To date, published animal models of SARS-CoV-2 infection during pregnancy have been limited (25, 41), which has hindered investigation into both host and viral factors that may underlie the severe outcomes observed in humans. Animal models have only been used to study the potential reproductive toxicity of nirmatrelvir in rats, rabbits, and zebrafish, with no evidence of embryonic toxicity, fetal abnormalities, maternal toxicity, or other adverse outcomes (42, 43). Whether equivalent dosing of nirmatrelvir administered during pregnancy is equally efficacious against SARS-CoV-2 infection in pregnant as in nonpregnant animals has not been reported.

In the current study, we developed a mouse model of SARS-CoV-2 infection during pregnancy to investigate maternal and offspring outcomes associated with severe COVID-19 disease during pregnancy and elucidate the contribution of gestational age, pulmonary and placental involvement in adverse outcomes, and control of virus replication. Further, we sought to assess the efficacy of ritonavir-boosted nirmatrelvir in limiting virus replication, preventing maternal disease, and mitigating observed adverse offspring outcomes. Our results demonstrate that SARS-CoV-2 infection during late gestation causes more severe maternal disease as well as impaired fetal growth and neurodevelopment than infections earlier in gestation, with maternal disease and fetal growth restriction associated with reduced pulmonary antiviral type-1–IFN responses, greater viral replication in the lungs, and loss of placental trophoblasts. Treatment with ritonavir-boosted nirmatrelvir not only reduced pulmonary virus replication but also prevented severe disease and adverse fetal growth and neurodevelopmental outcomes, highlighting additional benefits of antiviral treatment during pregnancy.

Results

Mouse adapted SARS-CoV-2 causes morbidity in pregnant mice, which increases with gestational age. To evaluate if SARS-CoV-2 caused greater disease in pregnant than nonpregnant mice and if maternal morbidity was impacted by gestational age, we intranasally inoculated outbred pregnant CD1 dams at E6, E10, or E16, roughly corresponding developmentally to human first, second, or third trimesters, respectively (44), or age-matched nonpregnant females with mouse adapted SARS-CoV-2 (maSCV2) (45) or media and measured body mass change as an indicator of morbidity. Nonpregnant females (Figure 1A) and dams infected at E6 (Figure 1B) experienced mild morbidity, losing notable body mass [i.e., approximately 10% of their initial body mass by 4 days postinfection (DPI)], but then appearing indistinguishable from mock-inoculated females by 7 DPI. In contrast, dams infected at E10 (Figure 1C) or E16 (Figure 1D) experienced prolonged maternal morbidity, with E10-infected dams gaining less body mass for the remainder of gestation than mock-inoculated dams (Figure 1C), and E16-infected dams failing to regain body mass for the remainder of gestation or during lactation compared with mock-inoculated dams (Figure 1D). No mortality was observed in any group. To compare the impact of gestation on maternal morbidity, the change in body mass relative to gestational-age matched mock-inoculated animals (Figure 1E) and cumulative clinical scores of disease (Figure 1F) were analyzed. maSCV2 infection of pregnant dams at E16 resulted in greater body mass loss and clinical disease than infection of either nonpregnant females or dams at either E6 or E10. Pregnancy and gestational age increase the severity of SARS-CoV-2 outcomes in mice, consistent with human COVID-19 data (1, 10).

Pregnant dams infected late in gestation have reduced IFN-β responses, increased viral load, and reduced pulmonary function after infection. Deficits in type-1–IFN signaling are associated with severe COVID-19 in people (46) and mice (47) who are not pregnant. Pregnancy is associated with downregulation of prototypical cytolytic and antiviral pathways, including type-I IFNs, and upregulation of antiinflammatory pathways toward mid to late gestation (48). We hypothesized that E16-infected dams would have a reduced type I IFN response after SARS-CoV-2 infection compared with E6-, and E10-infected dams and nonpregnant females. To test this, we infected pregnant dams at E6, E10, and E16 as well as age-matched nonpregnant females with maSCV2 or media and collected lungs at 3 DPI. Infected nonpregnant females as well as E6- and E10-infected dams had significantly greater concentrations of pulmonary IFN-β compared with matched mock-inoculated females (Figure 2A). In contrast, maSCV2 infection at E16 resulted in pulmonary concentrations of IFN-β that were indistinguishable from mock-inoculated dams and suppressed relative to either nonpregnant females, E6 dams, or E10 dams infected with maSCV2 (Figure 2A). To determine if reduced antiviral IFN-β concentrations were

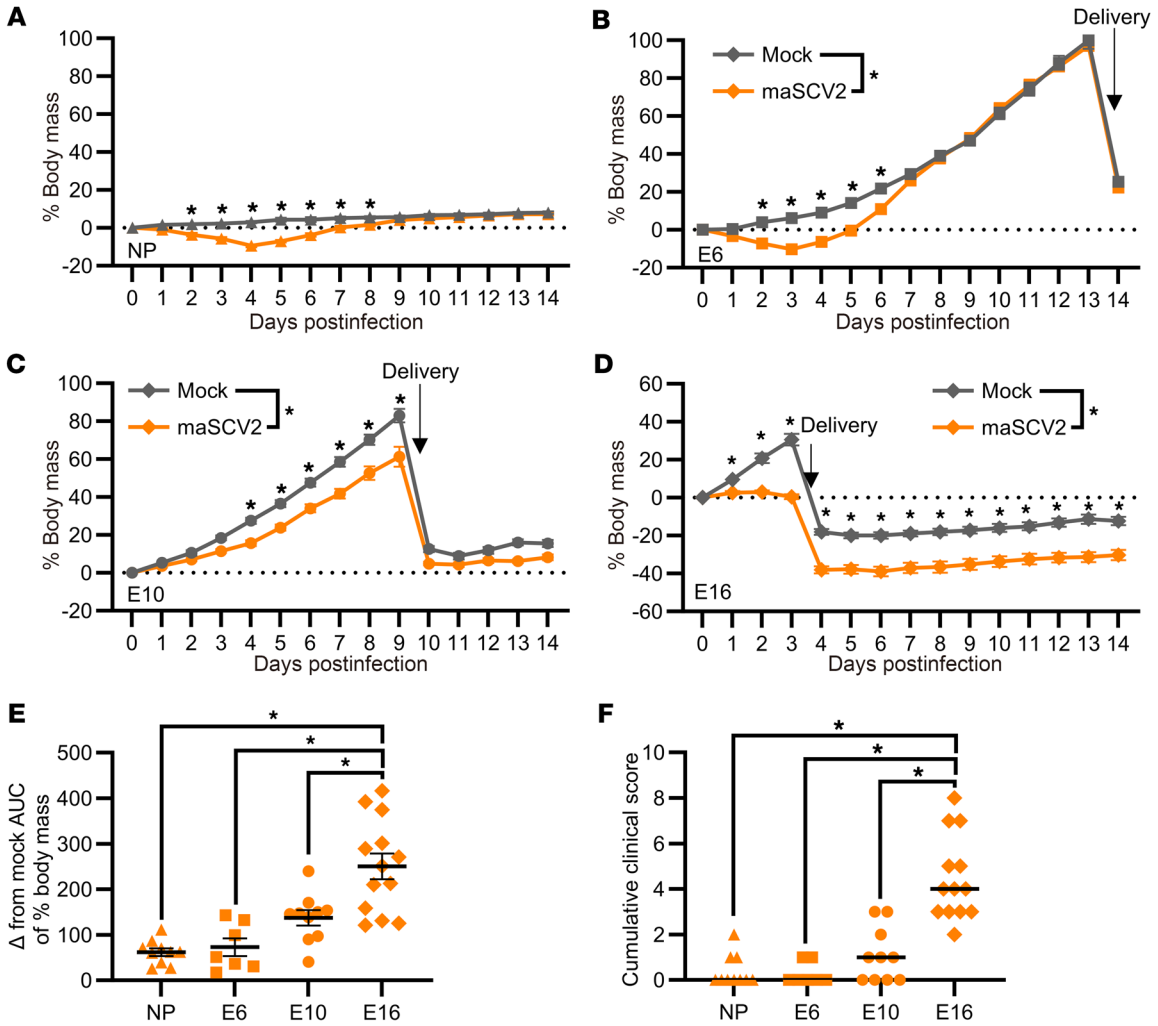

Figure 1. maSCV2 infection of pregnant dams results in gestation-dependent morbidity. Nonpregnant adult females (**A**) or dams at E6 (**B**), E10 (**C**), and E16 (**D**) were intranasally inoculated with 1×10^5 $TCID_{50}$ of a mouse adapted SARS-CoV-2 (maSCV2) or mock inoculated with media. Following infection, mice were monitored for change in body mass and clinical signs of disease over 14 days (**A**–**D**). AUC of body mass change curves for infected and uninfected animals were calculated, and then the AUC of infected animals was subtracted from the average AUC of mock animals of the same reproductive status and gestational age (**E**). Clinical scores given to animals included dyspnea, piloerection, hunched posture, and absence of an escape response and are quantified on a score of 0–4. The cumulative clinical score over the 14-day monitoring period is reported for each animal (**F**). Individual shapes (**A**–**D**) or bars (**E** and **F**) represent the mean (**A**–**E**) or median (**F**) ± SEM (**A**–**E**) from 2 independent replications (n = 7–13/group) with individual mice indicated by shapes (**E** and **F**). Statistical significance was determined by 2-way repeated measures ANOVA with Bonferroni posthoc test (**A**–**F**, to compare individual time points), 2 tailed unpaired t test of AUCs (**A**–**F**, to compare across all time points), 1-way ANOVA with Bonferroni posthoc test (**E**), or Kruskal-Wallis test (**F**). *$P < 0.05$.

associated with greater pulmonary virus replication at 3 DPI, we evaluated infectious viral titers (Figure 2B) and viral N1 gene copy numbers (Supplemental Table 1; supplemental material available online with this article; https://doi.org/10.1172/JCI170687DS1) in the lungs of nonpregnant, E6, E10, and E16 pregnant females that were maSCV2-infected. E16-infected dams had significantly greater pulmonary titers of infectious virus and viral RNA than either E6-infected dams, E10-infected dams, or infected nonpregnant females (Figure 2B and Supplemental Table 1).

To determine if greater viral replication contributed to worse pulmonary outcomes, at 3 DPI, we evaluated pulmonary histopathology (Figure 2, C and D and Supplemental Figure 1), and diffusion capacity (DF_{CO}; Figure 2E) in the lungs of nonpregnant, E6, or E16 pregnant females that were either maSCV2 or mock-infected. maSCV2 infection induced pulmonary histopathological changes, including intra-alveolar necrosis and inflammatory cell debris, and peribronchiolar, and perivascular mononuclear inflammatory infiltrates that were observed in nonpregnant (Supplemental Figure 1A, representative image), E6- (Supplemental Figure 1B, representative image), and E16- (Figure 2C, representative image) infected mice (Figure 2D, scoring) to equivalent levels. maSCV2 infection at E16 significantly reduced pulmonary function, as measured by DF_{CO}, which was not observed following maSCV2 infection at E6 or in nonpregnant females. These data suggest that late gestation is associated with reduced antiviral responses, greater virus replication, and reduced pulmonary function.

SARS-CoV-2 infection late in gestation disrupts trophoblasts and cytokine concentrations in the placenta. As placental pathology has

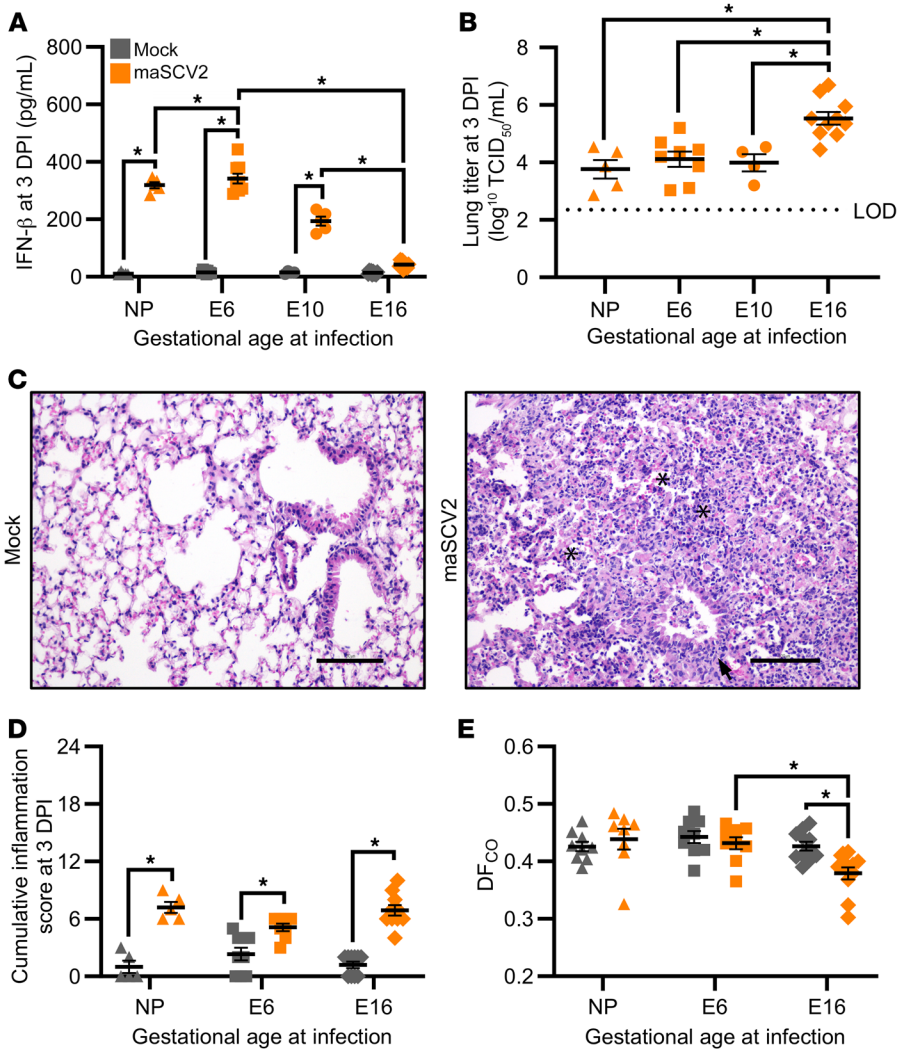

Figure 2. Pregnant dams infected during the third trimester equivalent have reduced IFN-β responses, increased viral load, and reduced pulmonary function after infection. Nonpregnant adult females or dams at E6, E10, and E16 were intranasally inoculated with 1×10^5 $TCID_{50}$ maSCV2 or mock inoculated with media and euthanized 3 days after infection (DPI) to collect maternal and fetal tissues. IFN-β and viral titers in the right cranial lungs were measured using ELISA (**A**) and $TCID_{50}$ assay (**B**), respectively. Sections of fixed left lungs were stained by H&E to evaluate lung inflammation and images were taken at ×20 magnification, with representative images of lungs maSCV2 or mock-inoculated at E16 shown (**C**). Asterisks (*) indicate intra-alveolar necrosis and inflammatory infiltrates, and arrows indicate peribronchiolar inflammatory infiltrates. Histopathological scoring was performed by a blinded board-certified veterinary pathologist to measure cumulative inflammation scores. Scale bar: 100 μm. (**D**) A subset of mice were tracheostomized at 3 DPI to measure pulmonary function through the diffusion capacity for carbon monoxide (DF_{CO}) before euthanasia (**E**). Bars represent the mean (**A**–**E**) ± SEM from at least 2 independent replications (n = 4–11/group) with individual mice indicated by shapes. Statistical significance was determined by 2-way ANOVA with Bonferroni posthoc test (**A**, **D**, **E**) or 1-way ANOVA with Bonferroni posthoc test (**B**). LOD, limit of detection. *$P < 0.05$

been observed during COVID-19 (49–51), we next investigated if maSCV2 could infect or cause damage to the placenta. Dams were mock- or maSCV2-infected at E10, when the placenta is formed (44), or E16 and euthanized at 3 DPI. Placentas, fetal tissues, and maternal sera were analyzed for infectious virus and viral RNA (Supplemental Table 1), with placentas further analyzed for tissue damage (Figure 3). All placentas, fetal tissues, and maternal sera were negative for viral RNA and infectious virus (Supplemental Table 1), consistent with human reports that direct placental infection and vertical transmission during COVID-19 is rare (23, 24). Despite no detectable infectious virus or viral RNA, placentas from E16-infected dams had reduced numbers of mononuclear trophoblast giant cells (Figure 3A for representative images, and Figure 3B for quantification), suggestive of damage to the trophoblast-endothelial cell barrier, which separates maternal and fetal blood in the labyrinth of the murine placenta (52). Staining for cytokeratin (trophoblasts, Figure 3, C and E, and Supplemental Figure 2A) and vimentin (endothelial cells, Figure 3, D and F and Supplemental Figure 2B) was performed and revealed a significant loss of trophoblasts, but not endothelial cells, in placentas from E16-infected compared with mock-infected dams (Figure 3, C–F). These data illustrate disruption of the maternal and fetal barrier in the absence of direct viral infection or vertical transmission. Moreover, cell numbers in placentas of E10-infected dams did not differ from placentas of mock-inoculated dams (Supplemental Figure 2, A and B). These data suggest that placental damage may be associated with the more severe maternal disease seen with infection at E16, potentially due to maternal immune activation or sickness behavior (53–55), which will require further studies for elucidation.

Altered concentrations of cytokines, including IFN-β and IL-1β, in the placenta are associated with placental damage (53, 56–58). As such, we measured IFN-β and IL-1β in placentas of dams that were maSCV2 infected or mock inoculated at E10 (Supplemental Figure 2, C and D) or E16 (Figure 3, G and H). Maternal maSCV2 infection at E16, but not E10, resulted in increased concentrations of IFN-β and reduced concentrations of IL-1β in the placenta relative to mock-inoculated dams (Figure 3, G and H and Supplemental Figure 2, C and D) These data suggest that maSCV2 infection shifted the balance of these 2 counter-regulatory cytokines in the placenta (59, 60), with placental IFN-β and IL-1β concentrations being correlated, regardless of infection status or timing of infection (Supplemental Figure 2E).

SARS-CoV-2 infection late in gestation causes intrauterine growth restriction. COVID-19 during human pregnancy is associated with

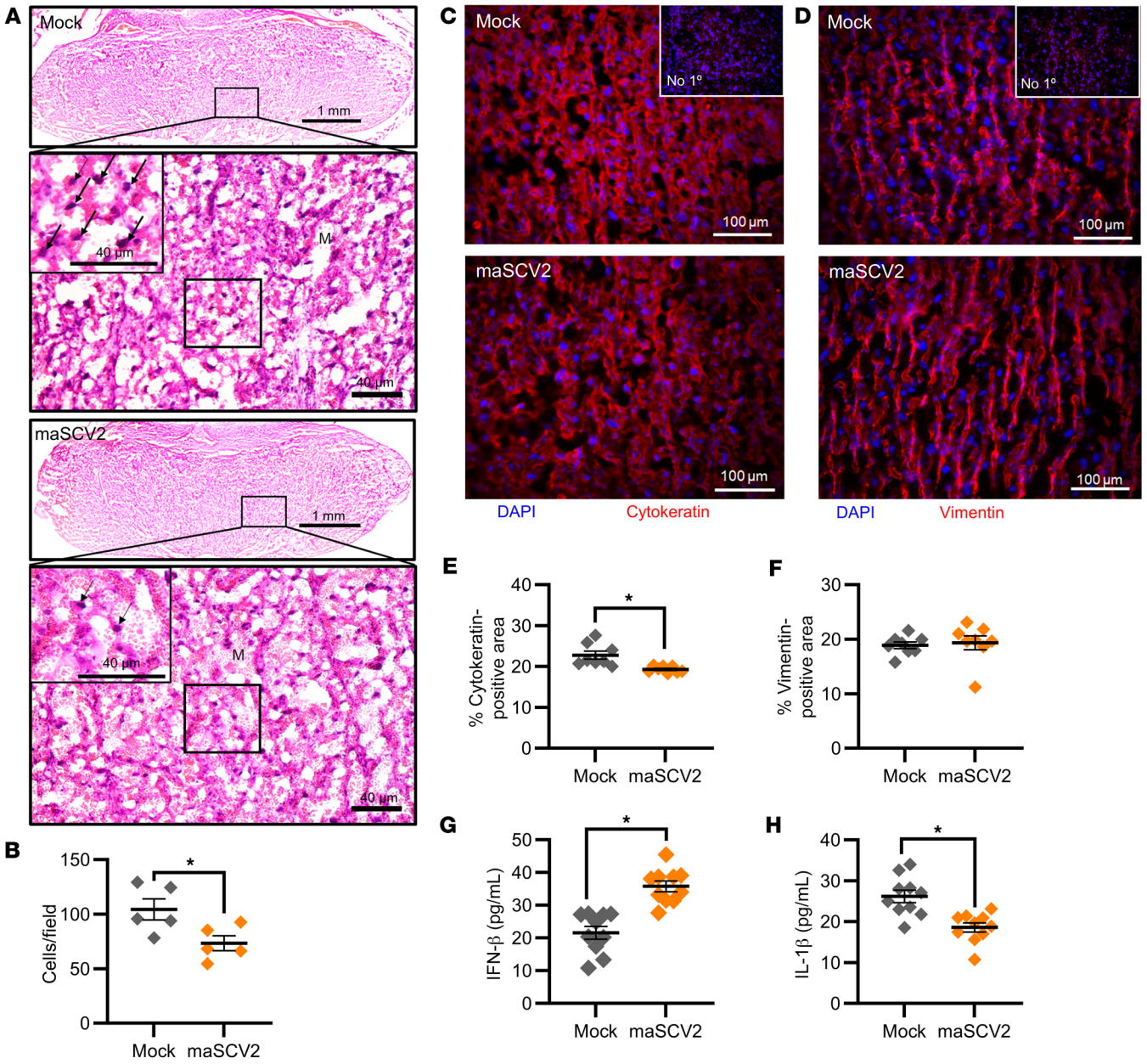

Figure 3. Third trimester–equivalent maSCV2 infection disrupts the trophoblast layer of the placental labyrinth zone and cytokine concentrations. At E16, pregnant dams were intranasally inoculated with 1×10^5 $TCID_{50}$ of maSCV2 or mock inoculated with media and euthanized at 3 DPI to collect placentas. Representative H&E images (**A**) were taken at ×5 (upper panels) and ×20 magnification (lower panels, and specific areas of interest further zoomed 1.75-fold (black box). Within H&E-stained placentas, arrows indicate trophoblast giant cells and the letter M in each lower panel indicates maternal blood spaces. Mononucleated trophoblast giant cells were identified and counted at ×20 magnification. Scale bars: 1mm (upper panels) and 40 μM (**A**, lower panels), (**B**). Placentas were immunostained for cytokeratin (**C**, red) to mark trophoblasts or vimentin (**D**, red) to mark endothelial cells and DAPI (blue) to label nuclei, with controls without primary antibody run in parallel. Representative images were taken at ×20 magnification. Quantification of the percentage positive area for each marker is shown (**E** and **F**). Placentas were homogenized and analyzed by ELISA for IFN-β (**G**) IL-1β (**H**). Bars represent the mean ± SEM (n = 5–10/group) with each shape indicating one placenta. For analysis of images, each shape is the mean quantification or count of 6 fields of view. Statistical significance was determined by unpaired 2 tailed t test. Scale bar: 100 μm (**C** and **D**). *$P < 0.05$.

adverse pregnancy and fetal outcomes including preterm birth, stillbirth, small size for gestational age, and reduced birth weight (15). To evaluate if the maSCV2-induced maternal morbidity and placental damage observed after infection at E16 was associated with adverse pregnancy or fetal outcomes, we inoculated dams with maSCV2 or media at E6, E10, or E16, with a subset of dams euthanized at 3 DPI to evaluate fetal viability and the remainder followed to evaluate birth outcomes. Neither fetal viability (Figure 4A) nor litter size (Figure 4B) was affected by maSCV2 infection during pregnancy at any gestational age. maSCV2 infection at E6 or E10 did not result in reductions in fetal growth relative to fetuses from mock-inoculated dams (Figure 4, C–E). In contrast,

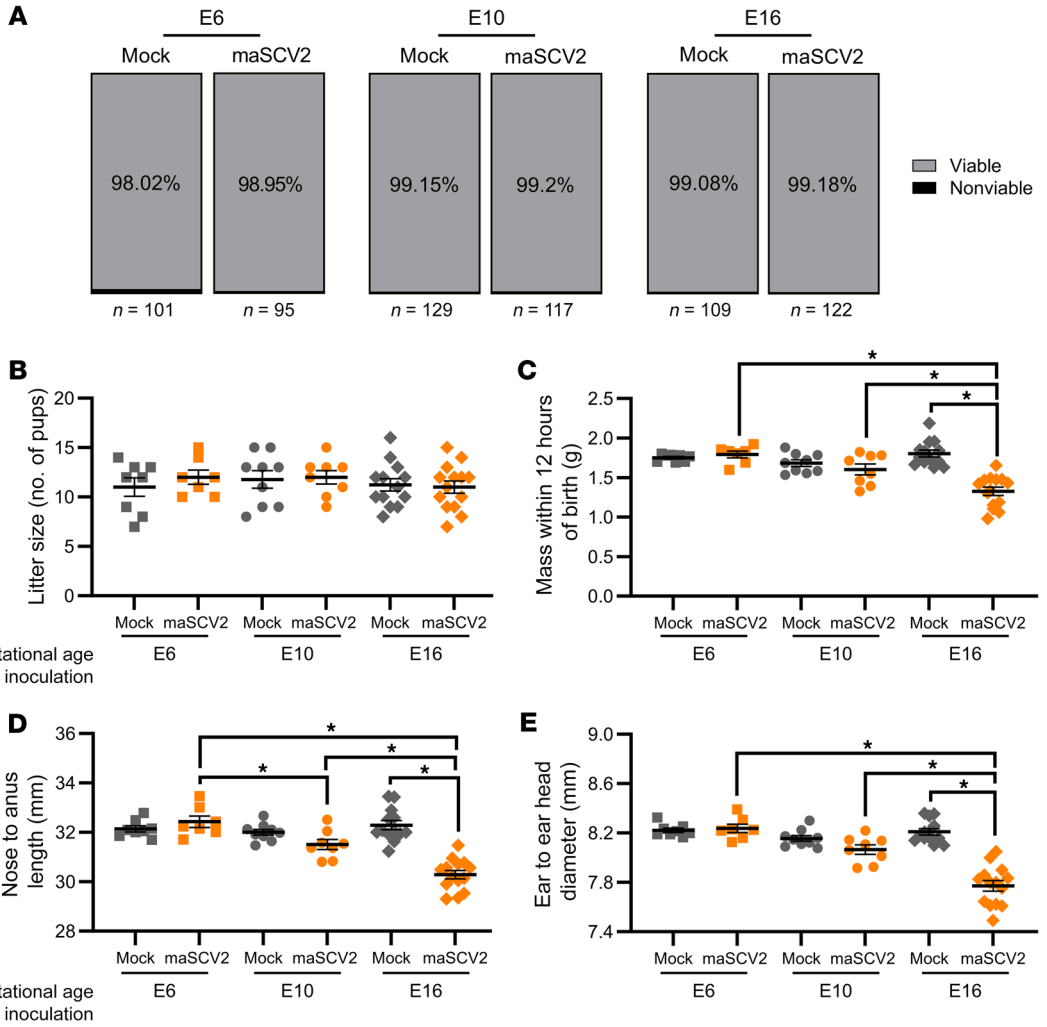

Figure 4. Third trimester-equivalent maSCV2 infection causes intrauterine growth restriction. At E6, E10, or E16, pregnant dams were intranasally inoculated with 1×10^5 $TCID_{50}$ of maSCV2 or mock inoculated with media. At 3 DPI, a subset of dams were euthanized, and fetal viability was determined as the percentage of fetuses within the uterus (**A**, *n* = total number of fetuses from 8–12 dams per group from 2 independent replicates). Fetuses were counted as nonviable if they were smaller or discolored compared with gestational age-matched live fetuses or if a fetus was absent at an implantation site. A subset of dams were followed into the postnatal period to characterize adverse birth outcomes. At postnatal day 0 (PND0) overall litter size (**B**), pup mass (**C**), pup body length (**D**), and pup head diameter (**E**) were measured. Average measurements of each independent litter were graphed (**B**–**E**). Bars represent the mean ± SEM from 2 independent replicates (*n* = 7–14/group) with the average of individual litters indicated by shapes. Statistical significance was determined by χ^2 (**A**) or 2-way ANOVA with Bonferroni posthoc test (**B**–**E**). $^*P < 0.05$.

maSCV2 infection at E16 led to statistically significantly smaller pups in terms of mass, length, and head size relative to fetuses from mock-infected dams (Figure 4, C–E). Collectively, fetuses from E16-infected dams had greater growth restriction than fetuses from either E6- or E10-infected dams (Figure 4, C–E). Reduced birth size was not mediated by preterm birth, as all dams, regardless of infection, delivered at approximately E20 (61). These data indicate that maSCV2 infection during the third trimester equivalent of pregnancy results in intrauterine growth restriction, which was not observed when infection occurred earlier during gestation.

Offspring of SARS-CoV-2 infection late in gestation display cortical thinning and reduced neurodevelopmental behaviors. In addition to adverse perinatal outcomes, COVID-19 during pregnancy also has been associated with an increased risk of neurodevelopmental disorders in infants within their first year of life (20, 21). As such, we evaluated offspring of mock-inoculated or maSCV2-infected dams at E16 for reduced cortical thickness at postnatal day (PND) 0 and delayed neurobehavioral function at PND 5. Offspring of E16-infected dams had significant cortical thinning compared with offspring from mock-inoculated dams (Figure 5, A and B), consistent with their reduced head diameter (Figure 4E). Offspring of E16-infected dams displayed delayed surface righting (Figure 5C), cliff aversion (Figure 5D), and negative geotaxis (Figure 5E) compared with offspring from mock-infected dams. Male offspring were more affected by maternal infection at E16 than female offspring, consistent with literature indicating that males are more severely impacted by in utero insults (62, 63), including SARS-CoV-2 infection (21). Offspring of dams that were either maSCV2- or mock-infected at E6 or E10 also were subjected to neurobehavioral testing, and no effect of either maternal infection

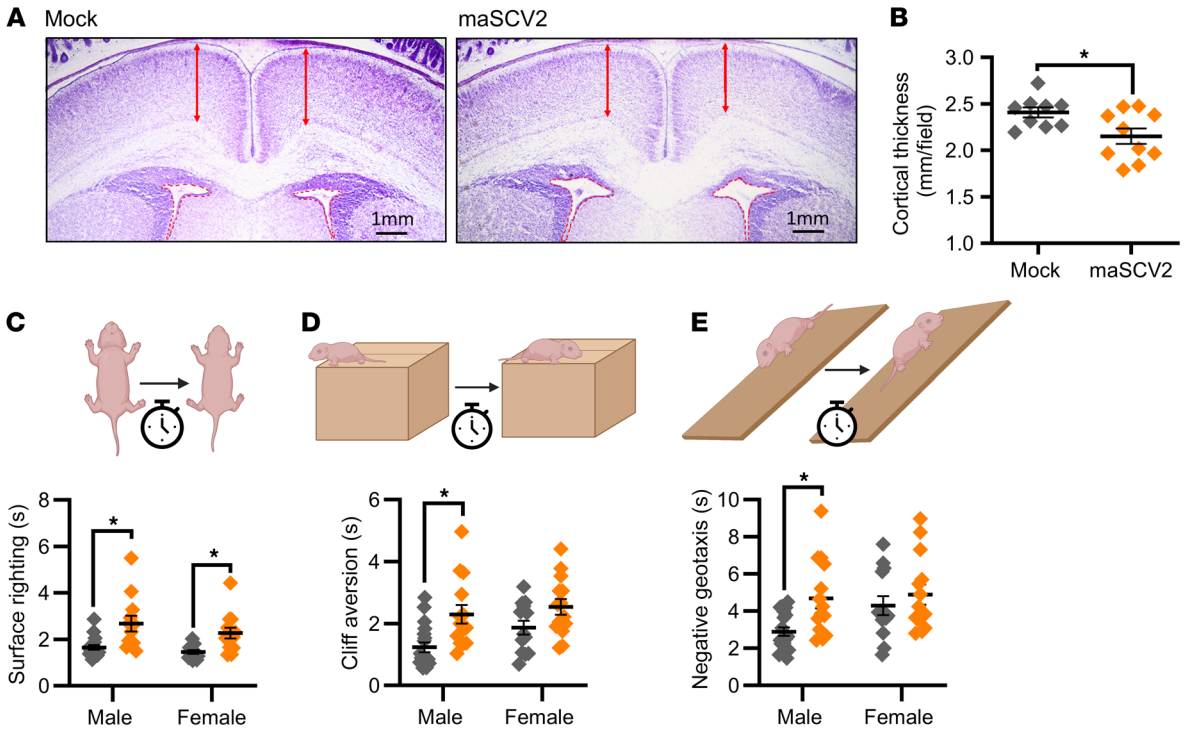

Figure 5. Offspring of dams infected with maSCV2 during the third trimester equivalent display cortical thinning and reduced neurodevelopmental function. At E16, pregnant dams were intranasally inoculated with 1×10^5 $TCID_{50}$ of maSCV2 or mock inoculated with media. At PND0, a randomly selected subset of pups were euthanized via decapitation to collect fetal heads, which were fixed, sliced, and Nissl stained. Cortical thickness (**A**, red arrows) was measured from both brain hemispheres per pup and quantified as the average of 10 measurements per pup, with a single pup randomly chosen per dam (**B**, *n* = 9–10 independent litters/group from 2 independent replicates). A subset of offspring were followed to PND5, sexed, and the neurobehavioral assays of surface righting (**C**), cliff aversion (**D**), and negative geotaxis (**E**) were performed to measure neurological development. 1–2 pups per sex per dam were subjected to each test, with 3 trials given per test, and each pup's best trial for each test was reported (**C**–**E**, *n* = 9–10 independent litters/group from 2 independent replicates). Bars represent the mean ± SEM with each shape indicating 1 pup. Statistical significance was determined by unpaired 2 tailed *t* test (**B**) or 2-way ANOVA with Bonferroni posthoc test (**C**–**E**). Graphics built with Biorender.com. $^*P < 0.05$.

or sex of offspring was observed (Supplemental Figure 3). These data highlight that infection with maSCV2 during the third trimester-equivalent of pregnancy causes both short and long-term adverse fetal outcomes, in the absence of vertical transmission and consistent with human literature (2, 20, 21).

Ritonavir-boosted nirmatrelvir treatment prevents morbidity and reduces pulmonary viral titers following SARS-CoV-2 infection late in gestation. Because of the increased risk of severe COVID-19 and adverse fetal outcomes, pregnant individuals are recommended to receive the antiviral ritonavir-boosted nirmatrelvir in the United States (33, 34). There are, however, limited data on its efficacy during pregnancy, with human and animal studies primarily focused on evaluating safety and toxicity (38, 42). Additionally, studies evaluating nirmatrelvir's efficacy in nonpregnant animals utilized high doses of nirmatrelvir alone in lieu of boosting with ritonavir (64, 65). To better reflect the doses administered to individuals who are pregnant, we first evaluated the efficacy of nirmatrelvir and ritonavir at doses calculated to be the mouse equivalent to a human doses (66) in nonpregnant females compared with high dose nirmatrelvir alone. Mouse equivalent dosing of nirmatrelvir and ritonavir was similar to high dose nirmatrelvir alone at preventing maSCV2 induced morbidity (Supplemental Figure 4A) and reducing pulmonary viral loads (Supplemental Figure 4B) in nonpregnant females. As CYP3A enzymes are responsible for the metabolism of nirmatrelvir (67), we evaluated liver CYP3A in pregnant dams at E16 and age-matched nonpregnant females and found no difference in total expression (Figure 6A; see complete unedited blots in the supplemental material), further supporting the use of mouse-equivalent doses of nirmatrelvir and ritonavir during pregnancy.

To evaluate the efficacy of ritonavir-boosted nirmatrelvir during pregnancy, we treated maSCV2 and mock-infected dams twice daily with mouse-equivalent doses of nirmatrelvir and ritonavir or vehicle for 5 days (68), starting at 4 hours after infection. maSCV2-infected dams treated with vehicle failed to gain mass during the remainder of pregnancy and had reduced mass compared with mock-inoculated dams through lactation (Figure 6B). In contrast, treatment of maSCV2-infected dams with ritonavir-boosted nirmatrelvir prevented maternal morbidity and resulted in morbidity AUCs that were equivalent to those of mock-inoculated dams (Figure 6B). Ritonavir-boosted nirmatrelvir did not significantly reduce infectious viral loads in the nasal turbinates of pregnant or nonpregnant females (Figure 6C). In the lungs, however, ritonavir-boosted nirmatrelvir reduced viral loads in pregnant, but not nonpregnant, females compared to vehicle-treated comparators, likely because infected

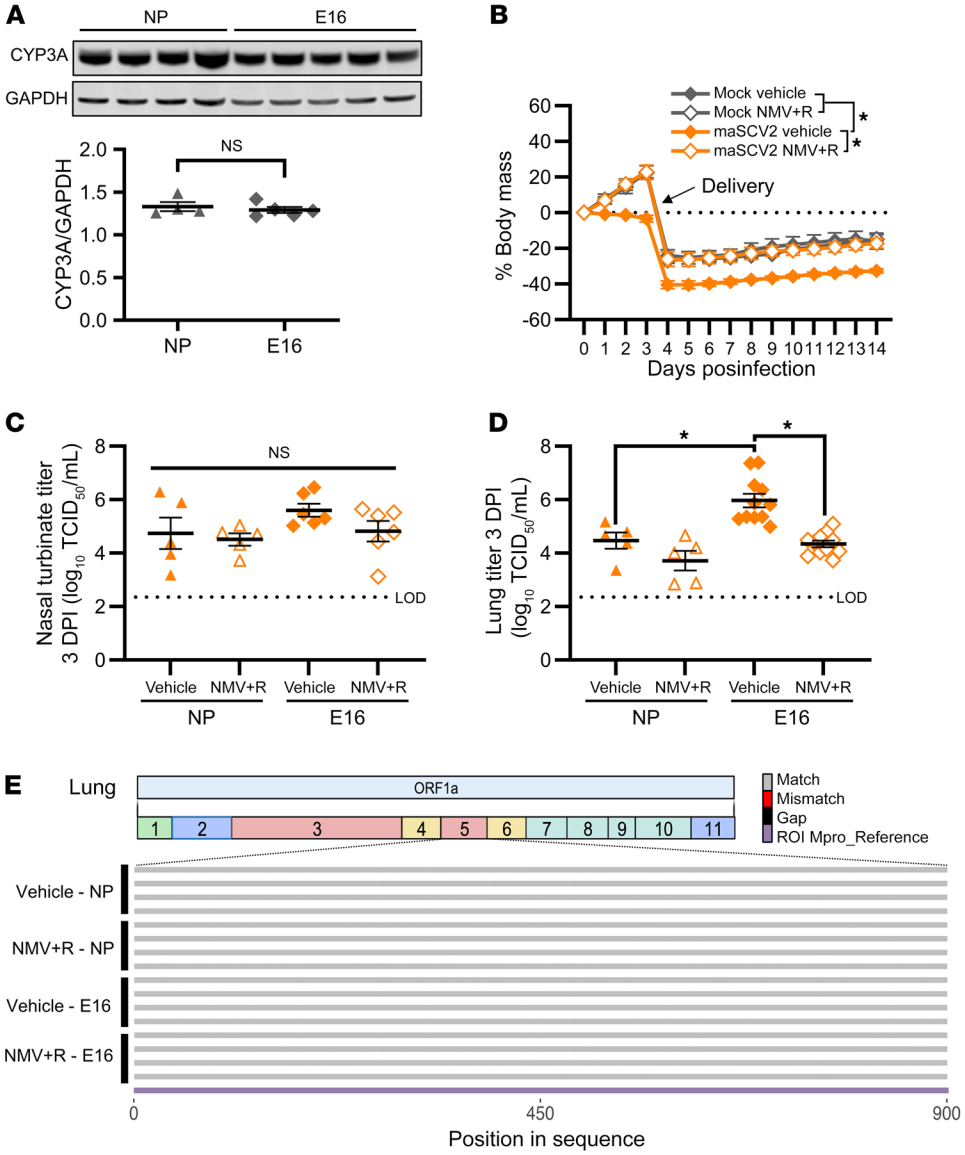

Figure 6. Ritonavir-boosted nirmatrelvir mitigates maternal morbidity and reduced viral titers in the lungs of pregnant dams. Uninfected adult nonpregnant and pregnant (E16) females were euthanized, liver tissue collected, and Western blots performed to quantify the amount of overall CYP3A expression (**A**, n = 4–5/group). At E16, pregnant dams or age-matched nonpregnant females were intranasally infected with 1×10^5 $TCID_{50}$ of maSCV2 or mock inoculated with media. Starting at 4 hours after infection and continuing twice daily for 5 days or until tissue collection, mice were treated with 1.7 mg nirmatrelvir and 0.6 mg ritonavir per dose or vehicle and were monitored for changes in body mass for 14 days (**B**, n = 6/group from 2 independent replicates). A subset of dams were euthanized at 3 DPI, nasal turbinate and lung tissue were collected, and viral titers were measured by $TCID_{50}$ assay (**C** and **D**, n = 5–11/group). RNA was extracted from lung homogenate, reverse transcribed using ProtoScript II First Strand cDNA Synthesis Kit, the M^{pro} region amplified, and Oxford Nanopore sequenced by Plasmidaurus. Consensus sequences were imported and aligned to M^{pro} using ClustalO v1.2.3 in Geneious Prime v2023.0.4. Alignments were imported into R v4.1.1., visualized, and annotated using seqvisR v0.2.5 (**E**, n = 4/group). Bars represent the mean ± SEM from 2 independent replications with individual mice indicated by shapes (**A**, **C**, and **D**). Statistical significance was determined by 2 tailed unpaired t test (**A**), 2-way ANOVA with Bonferroni post-hoc test of AUCs (**B**), or 2-way ANOVA with Bonferroni posthoc test (**C** and **D**). Sequence graphic built using Biorender.com. LOD, limit of detection. $^*P < 0.05$.

vehicle-treated nonpregnant females already had lower viral loads than infected pregnant vehicle-treated dams (Figure 6D). We next determined if treatment with ritonavir-boosted nirmatrelvir selected for mutations in the coding region corresponding to the gene that encodes for the SARS-CoV-2 MPRO protease. The sequences encoding M^{PRO} did not differ between viral RNA obtained from ritonavir-boosted nirmatrelvir–treated mice and vehicle-treated mice, regardless of either pregnancy status or tissue type (Figure 6E and Supplemental Figure 5), suggesting that ritonavir-boosted nirmatrelvir is not selecting for mutations that would potentially reduce its efficacy, at least by 3 DPI.

Ritonavir-boosted nirmatrelvir treatment prevents intrauterine growth restriction and neurobehavioral deficits induced by SARS-CoV-2 infection late in gestation. To evaluate if ritonavir-boosted nirmatrelvir prevented adverse fetal and offspring outcomes, offspring of E16-infected and mock-inoculated dams treated with ritonavir-boosted nirmatrelvir or vehicle were evaluated at birth and PND5. Offspring of maSCV2-infected dams treated with vehicle were significantly smaller than offspring of mock-inoculated dams in mass (Figure 7A), length (Figure 7B), and head diameter (Figure 7C) at birth and demonstrated significant delays in surface righting (Figure 7D), cliff aversion (Figure 7E), and negative geotaxis (Figure 7F) at PND5, with greater neurobehavioral delays in males than females (Figure 7, D–F). Offspring of maSCV2-infected dams treated with ritonavir-boosted nirmatrelvir, however, did not differ from offspring of mock-inoculated dams in any size measures at birth (Figure 7, A–C) or neurobehaviors at PND5 (Figure 7, D–F). Ritonavir-boosted nirmatrelvir treatment prevented maSCV2-induced intrauterine growth restriction and neurobehavioral deficits in both males and females. Offspring of mock-inoculated dams treated with ritonavir-boosted nirmatrelvir did not differ from offspring of mock-inoculated dams in any offspring measure (Figure 7, A–F), consistent with reproductive studies in rabbits, which did not find toxicity during pregnancy (42) Overall, these findings suggest that treatment with ritonavir-boosted nirmatrelvir during pregnancy can not only reduce maternal pulmonary viral load, but prevents maternal morbidity and mitigates adverse fetal and offspring outcomes.

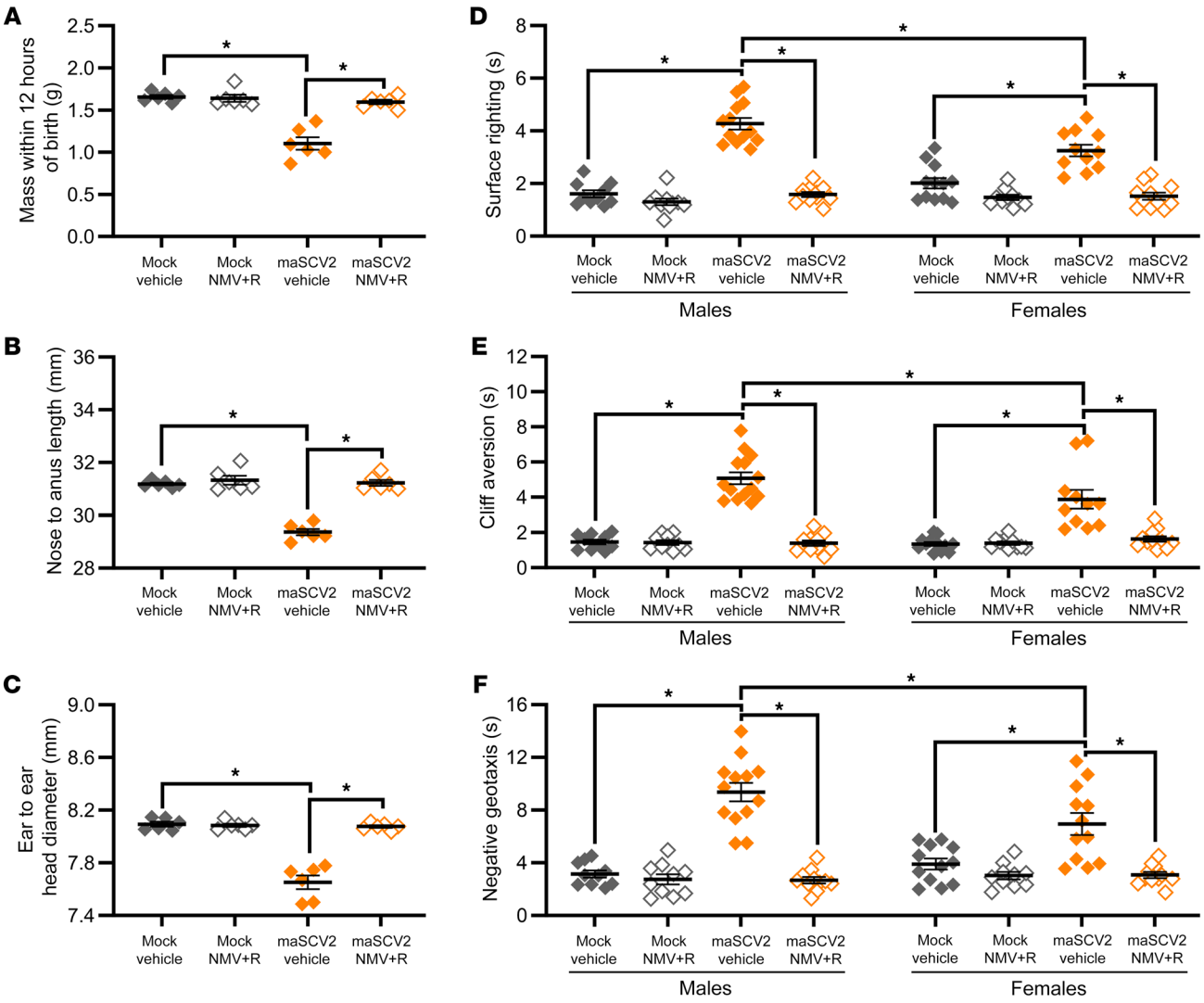

Figure 7. Ritonavir-boosted nirmatrelvir prevents adverse offspring birth outcomes and neurodevelopmental deficits associated with maternal maSCV2 infection. At E16, pregnant dams were intranasally inoculated with 1×10^5 $TCID_{50}$ of maSCV2 or mock inoculated with media. Starting at 4 hours after infection and continuing twice daily for 5 days or until tissue collection, mice were treated with 1.7 mg nirmatrelvir and 0.6 mg ritonavir per dose or vehicle. At PND0, a subset of pups were measured for pup mass (**A**), pup length (**B**), and pup head diameter (**C**). Average measurements of each litter were graphed (**A**–**C**, n = 6 independent litters/group from 2 independent replicates). A subset of offspring were followed to PND5, sexed, and the neurobehavioral assays of surface righting (**D**), cliff aversion (**E**), and negative geotaxis (**F**) were performed to measure neurological development. 1–2 pups per sex per dam were subjected to each test subsequently, with 3 trials given per test, and each pup's best trial for each test was reported (**D**–**F**, n = 6–8 independent litters/group from 2 independent replicates). Bars represent the mean ± SEM with each shape indicating one litter's average (**A**–**C**) or 1 pup (**D** and **E**). Statistical significance was determined by 2-way ANOVA with Bonferroni posthoc test (**A**–**C**) or 3-way ANOVA with Bonferroni posthoc test (**D**–**F**). *$P < 0.05$.

Discussion

Animal models of COVID-19 are powerful tools to study pathogenesis, consider risk-altering conditions such as pregnancy, and evaluate therapeutic interventions (69, 70). In the current study, we established a mouse model of SARS-CoV-2 infection during pregnancy that recapitulates many of the clinical findings of COVID-19 during human pregnancy. Pregnant dams infected with maSCV2 in late gestation experienced the most severe disease, exhibiting reduced pulmonary function and increased viral titers, while their offspring were small for gestational age and had neurodevelopmental delays. These findings are consistent with observations in humans where individuals who are pregnant with COVID-19, especially in mid-to-late gestation, have greater risk of severe disease, resulting in increased hospitalization and critical care admission (10, 11). Virological, biological, and social factors, including SARS-CoV-2 infectious dose and variant, preexisting immunity, and access to healthcare likely contribute to the diversity of adverse fetal outcomes observed with human COVID-19 during pregnancy (15, 18, 32, 71). Our mouse model does not account for all of these factors, which may explain the selective manifestation of adverse fetal outcomes, such as reduced birth mass and neurodevelopmental outcomes, that are worse in male than female offspring (16, 17, 20, 21). Our model did not capture other aspects of COVID-19 during pregnancy, including preterm birth or stillbirth (5, 15, 18, 22), that have been observed in human cases. Our results, therefore, have implications only for mecha-

nisms of fetal growth restriction and neurodevelopmental impairments seen in humans (16, 17, 20, 21).

At the maternal-fetal interface, intranasal maSCV2 infection resulted in placental alterations without direct virus infection, which is in accordance with the hallmarks of placental damage, inflammation, and maternal immune cell infiltration observed in placentas from mothers with COVID-19 during pregnancy (49–51). After characterizing the negative outcomes of maSCV2 infection in pregnancy, we used our model to assess the efficacy of ritonavir-boosted nirmatrelvir at a mouse-equivalent dose of what humans who are pregnant receive. This antiviral regimen was well tolerated by pregnant dams, reduced pulmonary virus titers, mitigated maternal morbidity, and prevented adverse offspring outcomes. Observational studies in human pregnancies indicate that ritonavir boosted-nirmatrelvir does not pose safety or toxicity risk to individuals who are pregnant (38), and may reduce COVID-19 symptoms without requiring additional medical interventions (39).

In addition to recapitulating aspects of human COVID-19 during pregnancy, our model identified a reduction in pulmonary IFN-β secretion after infection late in gestation and a corresponding increase in pulmonary viral titer as critical mediators of worse outcomes in late, compared with early, gestation. As deficits in type-1–IFN signaling have been associated with severe COVID-19 in both nonpregnant individuals (46) and mice (47), our data suggest that maternal morbidity may, in part, be due to an inability of pregnant dams to control viral replication because of a reduced type-1–IFN responses, particularly during late gestation. This potential mechanism of severe disease is consistent with immunological alterations of mouse and human pregnancy where the maternal immune response shifts to an antiinflammatory profile to support the semiallogenic fetus and diverts from antiviral and cytotoxic activity (12). Moreover, in human pregnancy, there is a documented decline in early antiviral effector cells and products including natural killer cells and type I IFNs (48).

The adverse maternal and fetal outcomes of SARS-CoV-2 infection during pregnancy are like those observed in other mouse models of viral pathogenesis during pregnancy including Zika virus (ZIKV) and influenza A virus (IAV) infection. Mouse models of ZIKV infection during pregnancy have shown that adverse fetal and neonatal outcomes including congenital abnormalities, reduced cortical thickness, and neurobehavioral deficits (72, 73), are mediated in part by transplacental virus transmission and acute placental inflammation (56, 72). While vertical transmission during ZIKV infection contributes to adverse outcomes, we and others have shown that the maternal immune response, including elevated production of IL-1β, also plays a key role in pathogenesis (72, 74). Vertical transmission of virus during COVID-19 is largely unseen in humans (23, 24, 50), and, in mice, the placental pathology following maSCV2 infection occurred without vertical transmission. These data further highlight that adverse neonatal outcomes are not exclusive to vertical transmission of viruses, but by maternal immune activation and damage at the maternal-fetal interface. Mouse models of IAV infection during pregnancy further demonstrate maternal morbidity and mortality, which is more severe in pregnant than nonpregnant animals (52, 55). Reduced type-I–IFN responses and greater viral loads in the lungs in pregnant dams late in gestation also have been observed in IAV infection (75), further supporting that pregnancy-associated suppression of type-I IFNs is a mechanism of severe maternal disease after respiratory virus infection.

Mouse models of viral infection during pregnancy are a valuable tool to assess the safety and efficacy of therapeutics to prevent adverse maternal and fetal outcomes. Our results support the efficacy of ritonavir-boosted nirmatrelvir for COVID-19 during pregnancy. While human studies of ritonavir-boosted nirmatrelvir during pregnancy are still needed, these findings provide a foundation for future human clinical trial design to include patients who are pregnant. Current approaches to assessing antiviral therapeutics in preclinical animal models include reproductive toxicity studies using supraphysiological doses but neglect to evaluate if pregnancy alters efficacy (42, 76, 77). Therefore, future preclinical models of antiviral therapies must be designed carefully to consider the complex interactions between pregnancy, viral pathogenesis, and drug pharmacokinetics. Mouse models of ZIKV antiviral treatment during pregnancy have illustrated the ability of maternal antiviral treatment to prevent vertical transmission to fetuses (78), a major adverse outcome associated with ZIKV infection during pregnancy. Individuals who are pregnant are largely excluded from clinical trials (29), which has contributed to a reduced uptake of antivirals and vaccines in pregnant populations, including COVID-19 therapeutics (79, 80). This exclusion is concerning because individuals who are pregnant and their neonates are highly vulnerable to many pathogens (81, 82). With further development of mouse models of viral infection and newly developed therapeutics in pregnancy, however, preclinical studies can guide clinical trial design and promote the inclusion of pregnant populations. By considering pregnancy in clinical trials, access and uptake of protective therapeutics during pregnancy can be improved.

Methods

Viruses and cells. The maSCV2, originally generated by Ralph Baric (University of North Carolina, Chapel Hill, North Carolina, United States) (45) was obtained from the Biodefense and Emerging Infections Research Resources Repository (BEI Resources no. NR-55329). The maSCV2 virus was originally generated via infectious clone technology using the sequence of SARS-CoV-2/human/USA/WA-CDC-02982586-001/2020 (WA1 strain) with added mutations in the Spike protein that were predicted to increase binding to murine ACE2 (83). This virus was further adapted to mice by sequential passage to generate increased virus replication and disease (45). Working stocks of maSCV2 virus were generated by infecting Vero-E6-TMPRSS2 (Japanese Collection of Research Bioresources Cell Bank no. JCRB1819) cells at a multiplicity of infection (MOI) of 0.01 tissue culture infectious dose 50 ($TCID_{50}$) per cell in infection media (DMEM; Sigma Aldrich) supplemented with 2.5% filter-sterilized FBS (Gibco), 100 U/mL penicillin and 100 μg/mL streptomycin (Gibco), 1 mM l-glutamine (Gibco), and 1-mM sodium pyruvate (Gibco). Approximately 72 hours after infection, the supernatant fluids were collected, clarified by centrifugation (400*g* for 10 minutes), and stored in aliquots at –70°C.

Experimental mice. Adult (8–12 weeks of age) timed pregnant and nonpregnant female CD-1 IGS mice were purchased from Charles River Laboratories. Pregnant mice arrived on E4, E8, and E14 and were singly housed, and nonpregnant female mice were housed at 5 per

cage before and after inoculation. Mice were housed under standard animal biosafety level 3 (ABSL3) housing conditions with ad libitum food and water. Mice were given at least 24 hours to acclimate to the ABSL3 facility prior to infections (84). All monitoring and experimental procedures were performed at the same time each day.

SCV2 infections and monitoring. All animal experiments and procedures took place in an ABSL3 facility at the Johns Hopkins School of Medicine. Experimental pregnant mice were intranasally infected at E6, E10, or E16 with 1×10^5 $TCID_{50}$ of maSCV2 (45) in 30 μL of DMEM (Sigma Aldrich) or mock inoculated with 30 μL of media. Dose-response studies in nonpregnant inbred female mice indicate that maSCV2 requires doses of 1×10^4 or 1×10^5 $TCID_{50}$ to cause disease in adult mice (45). Before intranasal infection, mice were anesthetized via intraperitoneal ketamine/xylazine cocktail (80 mg/kg ketamine, 5 mg/kg xylazine). Following intranasal infections, body mass and clinical signs of disease were monitored once daily in the morning for 14 days or until tissue collection. Clinical scores, determined in the home cage, were administered to mice on a scale of 0–4, with 1 point given for piloerection, dyspnea, hunched posture, and absence of an escape response on each day (85, 86). Clinical scores over the course of 14 days for each animal were summed to give a cumulative clinical disease score.

Antiviral treatment. Experimental animals were administered vehicle alone [1% (w/v) Soluplus (BASF), 1% (w/v) Tween 80 (Sigma Aldrich), 0.5% (w/v) methylcellulose (Sigma Aldrich) in purified water], high dose nirmatrelvir alone (300mg/kg; MedChem Express), or an animal equivalent dose of nirmatrelvir boosted with ritonavir (1.7 mg nirmatrelvir/dose [MedChem Express], 0.6 mg ritonavir/dose [Sigma Aldrich]). Animal equivalent doses were calculated as described (66) by converting the standard human dose of nirmatrelvir and ritonavir (68) to a body-surface-area equivalent for mice (66) using a standardized body surface area for mice of 0.007 mg/m^2, which is recommended for conversion of animal doses to human equivalent doses (87), along with an assumed mass of 30 g for all calculations so that pregnant and nonpregnant animals receive the same amount per dose. Mice were administered treatment via oral gavage twice daily for 5 days or until tissue collection, starting 4 hours after infection as described in the original published preclinical study of nirmatrelvir (64).

Offspring measurements and behavior. Offspring from mock inoculated dams and maSCV2 infected dams were measured at PND0, within 12 hours of birth. Body mass (g), length measured from nose to anus (mm), and head diameter measured from ear to ear (mm) were recorded for each pup directly, using a caliper, and the average for each independent litter was calculated to avoid confounding litter effects. Pups at PND5 were subjected to developmental neurobehavioral assays of surface righting, cliff aversion, and negative geotaxis as described (72, 88). For each test, 1 or 2 male and 1 or 2 female offspring from at least 5 independent litters were used per condition to avoid confounding litter effects. Pups were subjected to 3 attempts at each test, with the time to complete each test recorded on a stopwatch. The upper limit of time was 60 seconds, 30 seconds, and 60 seconds for surface righting, cliff aversion, and negative geotaxis, respectively. The pups' best trial for each test was used for analysis.

Diffusion capacity of carbon monoxide. To measure lung function of experimental mice, diffusion capacity for carbon monoxide (DF_{CO}) was measured. Modifications to a previously published protocol (89) were made for application in ABSL3. Mice were anesthetized with ketamine/xylazine cocktail (80 mg/kg ketamine, 5 mg/kg xylazine). Mice were tracheostomized with an 18-G stub needle. For each mouse, 2 3-mL syringes containing 0.8 mL of approximately 0.5% neon (Ne, an insoluble inert tracer gas), approximately 0.5% CO, and balanced air were prefilled and sealed with a 4-way stop cock. Following tracheostomy, gas was injected into the tracheostomy stub-needle to inflate the lungs for 2 seconds and held for 8 seconds. After 8 seconds, the 0.8 mL volume was withdrawn back into the syringe in 2 seconds and the syringe's stop cock closed, then the gas in the syringe was diluted to 2 mL with room air and resealed. This was repeated using the second syringe for each mouse. Mice were euthanized via cervical dislocation. The closed syringes were decontaminated in an oven at 75°C for 15 minutes within the ABSL3 to inactivate any virus in the gas sample. DF_{CO} was measured using gas chromatography as previously described (89).

Tissue and serum collection. Experimental dams (infected at E6, E10, or E16) or nonpregnant female mice were euthanized at 3 days after infection. Mice were anesthetized via isoflurane and exsanguination was preformed via cardiac puncture. At the time of euthanasia, the total number of viable and nonviable fetuses was quantified for each pregnant dam. Fetal viability was determined as the percentage of fetuses within uterine horns that were viable. Fetuses were counted as nonviable if they were smaller or discolored compared with gestational age-matched live fetuses or if a fetus was absent at an implantation site (56, 72, 73). Maternal lungs were collected, separated by lobe, and flash frozen on dry ice for homogenization. The left lung was inflated and fixed in zinc buffered formalin (Thermo Fisher Scientific) for at least 72 hours in preparation for histology. Fetuses and placenta were flash frozen in dry ice or fixed in 4% paraformaldehyde (Thermo Fisher Scientific) for 72 hours at 4°C for IHC. Serum was separated by blood centrifugation at 2,400*g* for 30 minutes at 4°C. A subset of uninfected pregnant (E16) and nonpregnant adult mice were euthanized and the median liver lobe was collected and flash frozen in dry ice for Western blotting.

Pulmonary histopathology. Fixed lungs were sliced into 3-mm blocks, embedded in paraffin, sectioned to 5 μm, mounted on glass slides, and stained with H&E solution to evaluate lung inflammation. Semiquantitative histopathological scoring was performed by a board-certified veterinary pathologist, blinded to study group assignments and outcomes, to measure both severity of inflammation and the extent of inflammation (90–92). Severity of perivascular and peribronchiolar mononuclear inflammation was scored on a scale of 0–4 (0, no inflammation; 1, 1 cell layer; 2, 2–3 cell layers; 3, 4–5 cell layers; 4, > 5 cell layers). Severity of alveolar inflammation was scored on a scale of 0–4 (0, no inflammation; 1, increased inflammatory cells in alveoli, septa clearly distinguished; 2, inflammatory cells fill alveoli, septa clearly distinguished; 3, inflammatory cells fill multiple adjacent alveoli, septa difficult to distinguish; 4, inflammatory cells fill multiple adjacent alveoli with septal necrosis). Extent of inflammation was scored separately for perivascular, peribronchiolar, and alveolar areas on a scale of 0–4 (0, no inflammation; 1, 2%–25% tissue affected; 2, up to 50% tissue affected; 3, up to 75% tissue affected; 4, > 75% of tissue affected). Individual scores were summed to give a cumulative inflammation score.

Infectious virus and viral genome copy number quantification and tissue inactivation. Frozen right cranial lungs, nasal turbinates, placentas, and fetuses were homogenized in lysing matrix D bead tubes (MP Biomedicals). Homogenization media (500mL DMEM [Sigma],

5mL penicillin/streptomycin [Gibco]) was added to bead tubes containing tissue at a minimum volume of 400 μL and maximum volume of 1200 μL (10% w/v) and homogenized at 4.0 m/s for 45 seconds in a MP Fast-prep 24 5G instrument. After homogenization, the supernatant was divided in half and transferred to 2 new microcentrifuge tubes. Triton X-100 was added to one of the transferred supernatants to a final concentration of 0.5% and incubated at room temperature for 30 minutes to inactivate maSCV2. Infectious and inactivated homogenates were stored at –80°C. Infectious virus titers in tissue homogenate or sera were determined by $TCID_{50}$ assay. Tissue homogenates or sera were serially diluted in infection media in sextuplicate into 96-well plates confluent with Vero-E6-TMPRSS2 cells, incubated at 37°C for 6 days. After incubation, 10% neutral buffered formalin was added to all wells to fix cells prior to staining and left overnight. Formalin was discarded and the plates were stained with naphthol blue black stain for visualization. Infectious virus titers were determined via the Reed and Muench method. Viral RNA copy number was determined by quantitative PCR (qPCR). A 200 μL aliquot of tissue homogenate or serum was mixed with 1 mL of TRIzol reagent (Invitrogen) for RNA extraction. To this, 200 μL of chloroform (Thermo Fisher Scientific) was added, followed by centrifugation at 12,000*g* for 15 minutes at 4°C. The clear supernatant was collected and an equal volume of 100% isopropyl alcohol (Thermo Fisher Scientific) was added. This mixture was centrifuged at 12,000*g* for 10 minutes at 4°C. The resulting RNA pellet was washed with 75% ethanol (Thermo Fisher Scientific), air dried, and resuspended in 50 μL of nuclease-free water. The real time qPCR for SARS-CoV-2 N1 gene detection was carried out by adding 2.5 μL of the isolated RNA into a master mix composed of 2.5 μL TaqPath 1-Step Multiplex Master Mix (Applied Biosystems), 0.75 μL of N1 SARS-CoV-2 RUO qPCR Primer & Probe Kit (IDT), and 4.25 μL of nuclease-free water. This mix was added to each well of a MicroAmp Optical 384-Well Reaction Plate (Applied Biosystems). Serial dilutions of N1 were prepared in 10-fold increments for absolute quantification of copy number. Each sample and standard were run in duplicate. The QuantStudio 12K Flex Real-Time PCR System (Applied Biosystems) was used for amplification, and data analysis was performed using the Design & Analysis Software 2.6.0 to identify SARS-CoV-2 N1.

Placental histology and IHC. Placentas were fixed for 72 hours at 4°C in 4% PFA in the ABSL3. Placentas were washed 5 times with PBS and immersed in 30% sucrose until saturation. Using a Leica CM1950 cryostat, the specimens were cut at 20-μm thickness and mounted on positively charged slides (Thermo Fisher Scientific). Routine H&E staining was performed to evaluate the morphological change of the placentas. Within H&E-stained sections, mononucleated trophoblast giant cells, distinguished by their large size and the presence of a single condensed dark blue-purple stained nucleus, were identified and counted under a magnification of ×20. For each placenta, 6 random images in the labyrinth at the middle level (thickest) of placenta were taken and the count was averaged. For IHC staining, slides were washed with PBS, which was followed by permeabilization in PBS solution containing 0.05% Triton X-100 and 10% normal goat serum (Invitrogen) for 30 minutes. Placentas were incubated with rabbit anti-vimentin (1:200, Abcam no. ab92547), or rabbit anti-cytokeratin (1:200, Dako no. Z0622) overnight at 4°C. The next day, sections were rinsed with PBS and then incubated with donkey anti-rabbit (Thermo Fisher Scientific no. R37119) fluorescent secondary antibodies (Thermo Fisher Scientific no. R37115) diluted 1:500 for 3 hours at room temperature. DAPI (Roche) was applied for counterstaining, followed by mounting with Fluoromount-G (eBioscience). Images were taken using a Zeiss Axioplan 2 microscope (Jena, Germany) under magnification ×5 or ×20. Cell density of vimentin- and cytokeratin-positive cell quantification was performed using Image J (1.47v). The ×20 images were captured from the same batch of experiments, utilizing identical imaging parameters, including exposure time for quantification. After setting the appropriate scale and threshold for positive expression, the percentage of positive expression relative to the entire area was calculated. For each placenta, 6 random images in the labyrinth at the middle level (thickest) of placenta were taken, and the average fluorescent area calculated for that placenta. One placenta per dam was used and 4–5 dams per group were analyzed.

Cortical thickness measurement. A subset of offspring was randomly selected to be euthanized via decapitation at PND0 and heads were fixed for 72 hours at 4°C in 4% PFA in the ABSL3. Fetal heads were washed 5 times with PBS and immersed in 30% sucrose until saturation. Using a Leica CM1950 cryostat, the specimens were cut at 20-μm thickness and mounted on positively charged slides (Thermo Fisher Scientific). Nissl staining was performed, and images were taken under ×5 magnification using a Canon EOS Rebel (Tokyo, Japan). Coronal cortical thickness was measured from 5 random sections at the striatum level of each neonatal brain, as previously described (73). Cortical thickness was measured from both brain hemispheres in each section using ImageJ software, and the average of 10 measurements per specimen was presented. Quantification shown represents the average measurement from a single randomly chosen pup for each dam (73).

IFN-β and IL-1β ELISA. IFN-β in inactivated right cranial lung or placental homogenate was measured by ELISA according to the manufacturer's protocol (PBL Assay Science). IL-1β in inactivated placental homogenate was measured by ELISA according to the manufacturer's protocol (Abcam).

Western blot. Flash frozen median liver lobes were homogenized in 1X Cell lysis Buffer (Cell Signaling Technology) with 1× Protease Inhibitor cocktail (Sigma Aldrich) and sodium fluoride (Thermo Fisher Scientific) at 20 μL lysis buffer per mg tissue. Protein lysates were stored at –80°C until analysis. Protein concentration of each lysate was measured using the Pierce BCA Protein Assay Kit (Thermo Fisher Scientific). For each sample, 20 μg of protein was subjected to SDS-polyacrylamide gel electrophoresis (SDS-PAGE) on NuPAGE 4%–12% Bis-Tris gels (Thermo Fisher Scientific). The gel was blotted onto Immobilon-FL PVDF Membrane (Millipore) and the membranes were blocked with a 1:1 mixture of 1XPBS/Tween-20 solution (Sigma Aldrich) and Intercept blocking buffer (LI-COR Biosciences) for 30 minutes at room temperature. Membranes were treated with a primary antibody diluted in blocking solution at 4°C overnight on a rocker. Membranes were then washed with PBS-Tween 3 times and incubated in secondary antibody solutions for 1 hour at room temperature on a rocker. Membranes were washed 3 times in PBS-Tween and then imaged on a ProteinSimple FluoroChem Q imager. Individual bands were quantified using Image Studio software (LI-COR Biosciences; version 3.1.4) The signal from each band was normalized against the GAPDH signal and graphed as arbitrary units. Primary antibodies used were rabbit anti-P450 3A4/CYP3A4 (Abcam no. ab3572) and mouse anti-GAPDH (Abcam no. ab82450). Secondary antibodies

included goat anti- mouse Alexa Fluor 488 (Thermo Fisher Scientific no. A11001) and donkey anti-rabbit Alexa Fluor Plus 647 (Thermo Fisher Scientific no. A32795).

Viral RNA extraction, sequencing, and analysis. For each sample, 200 μL of right cranial lung or nasal turbinate homogenate was mixed with 1 mL of TRIzol (Invitrogen), followed by 200 μL of chloroform (Fisher Scientific) to extract RNA and centrifuged at 12,000*g* for 15 minutes at 4°C. The clear portion of the supernatant was then pelleted at 12,000*g* for 10 minutes along with 500 μL of 100% isopropyl alcohol (Thermo Fisher Scientific) at 4°C. Pelleted RNA was then washed with 75% of ethanol (Thermo Fisher Scientific), air dried and resuspended in 20 μL of nuclease-free water. Reverse transcription was carried out using ProtoScript II First Strand cDNA Synthesis Kit (New England Biolabs) with random hexamer mix. The Mpro region was then amplified using forward primer 5′ ACAAAGATAGCACTTAAGGGTGG 3′ and reverse primer 5′ GCGAGCTCTATTCTTTGCACTAA 3′ and Oxford Nanopore sequenced by Plasmidsaurus (SNPsaurus LLC). Consensus sequences for lung and turbinate virus isolates were imported and aligned to Mpro ORF (NC_045512.2) using ClustalO v1.2.3 in Geneious Prime v2023.0.4. Alignments were imported into R v4.1.1, visualized, and annotated using seqvisR v0.2.5. ORF1a, and nonstructural protein annotation was visualized using BioRender. Raw FASTQ files for Mpro sequencing has been deposited through SRA under Bio Project All raw data for tiled amplicon sequencing performed for SARS-CoV-2 genome analysis in this study are deposited under BioProject: PRJNA940500 (SRA Numbers: SRX19551746-SRX19551765).

Statistics. Postinfection body mass changes were plotted and the AUC was calculated to provide individual data points that captured change over time, with AUCs compared with either 2-tailed unpaired *t* test or 2-way ANOVA followed by posthoc Bonferroni multiple comparisons tests. To compare body mass changes across gestational ages, individual AUCs were subtracted from the average AUC of mock mice at the same gestational age, with the difference from mock AUC compared with 2-way ANOVAs followed by posthoc Bonferroni multiple comparisons test. Cumulative clinical scores were analyzed using the Kruskal-Wallis test. Viral titers in lungs from infected dams were analyzed using 1-way or 2-way ANOVAs followed by posthoc Bonferroni multiple comparisons test. Western blot quantification, IHC quantification, and cortical thickness measurements were analyzed with 2-tailed unpaired *t* tests. Cumulative inflammation scoring, DFCO, IFN-β, and fetal measurements were analyzed with 2-way ANOVAs followed by posthoc Bonferroni multiple comparisons test. Pup neurodevelopment results were analyzed with 2-way or 3-way ANOVAs followed by posthoc Bonferroni multiple comparisons test. Fetal viability data were analyzed with a χ^2 test. Data are presented as mean ± SEM or as the median (cumulative clinical score). Mean or median differences were considered statistically significant at $P < 0.05$. Statistical analyses were performed using GraphPad Prism v9.5 (GraphPad Software).

Study approval. All animal procedures were approved by the Johns Hopkins University Animal Care and Use Committee (MO21H246). SARS-CoV-2 was handled in a BSL-3 containment facility using an institution -approved biosafety protocol (P2003120104).

Data availability. All raw data for tiled amplicon sequencing performed for SARS-CoV-2 genome analysis in this study are deposited under BioProject: PRJNA940500 (SRA Numbers: SRX19551746-SRX19551765). Other data supporting the conclusions of this article are available in the Supporting data values.

Author contributions

SLK, AP, IB, PSC, and JLP conceptualized and designed the experiments. PSC and JLP performed animal experiments. AP, WZ, and RZ grew and quantified viruses and homogenized and inactivated tissue. PSC and JLP performed ELISA and Western blots. KRM imaged and scored lung histology slides. PSC, JLP, WHR, and WM performed DFco analysis. JL and AL stained, imaged, and analyzed placental and fetal head tissue. EHA analyzed sequencing data. PSC and JLP statistically analyzed and graphed data. PSC, JLP, and SLK wrote the manuscript with input from all authors. All authors read and provided edits to drafts and approved the final submission. The order of authors, including co–first authors, was determined based on contributions to the overall design, experimentation, analyses, and writing.

Acknowledgments

The authors would like to thank Ralph Baric as well as the Klein, Pekosz, Davis, and Baumgarth laboratories for discussions about these data, Ariana Campbell for early assistance with animal studies, and Yan Zhao for help with viral RNA analysis. We would also like to thank Jason Villano and the expert animal care staff at the Johns Hopkins School of Medicine for assistance with maintenance of SARS-CoV-2-infected dams. Funding was provided by NIH/NICHD R01HD097608 (to IB and SLK), NIH/NIAID training grant T32AI007417-26 (to PSC and EHA), and NIAID N7593021C00045 (to AP).

Address correspondence to: Sabra L. Klein, 615 N. Wolfe Street, Room W2118, Baltimore, Maryland 21205, USA; Phone: 410.955.8898; Email: sklein2@jhu.edu. Or to: Andrew Pekosz, 615 N. Wolfe Street, Room W2116, Baltimore, Maryland 21205, USA. Phone: 410.502.9306; Email: apekosz1@jhu.edu. Or to: Irina Burd, 22 S. Greene Street St, Baltimore, Maryland 21201, USA; Phone: 410.328.5960; Email: iburd@som.umaryland.edu.

1. Lokken EM, et al. Disease severity, pregnancy outcomes, and maternal deaths among pregnant patients with severe acute respiratory syndrome coronavirus 2 infection in Washington State. *Am J Obstet Gynecol*. 2021;225(1):77.
2. Woodworth KR, et al. Birth and infant outcomes following laboratory-confirmed SARS-CoV-2 infection in pregnancy - SET-NET, 16 Jurisdictions, March 29-October 14, 2020. *MMWR Morb Mortal Wkly Rep*. 2020;69(44):1635–1640.
3. Laura ASC, et al. Reduced control of SARS-CoV-2 infection is associated with lower mucosal antibody responses in pregnant women [preprint]. https://doi.org/10.1101/2023.03.19.23287456. Posted on medRxiv March 20, 2023.
4. Zambrano LD, et al. Update: characteristics of symptomatic women of reproductive age with laboratory-confirmed SARS-CoV-2 Infection by Pregnancy Status - United States, January 22-October 3, 2020. *MMWR Morb Mortal Wkly Rep*. 2020;69(44):1641–1647.
5. Allotey J, et al. Clinical manifestations, risk factors, and maternal and perinatal outcomes of coronavirus disease 2019 in pregnancy: living systematic review and meta-analysis. *BMJ*. 2020;370:m3320.
6. Metz TD, et al. Disease severity and perinatal outcomes of pregnant patients with Coronavirus Disease 2019 (COVID-19). *Obstet Gynecol*. 2021;137(4):571–580.
7. Mullins E, et al. Pregnancy and neonatal outcomes of COVID-19: coreporting of common outcomes from PAN-COVID and AAP-SONPM

registries. *Ultrasound Obstet Gynecol*. 2021;57(4):573–581.
8. Jering KS, et al. Clinical characteristics and outcomes of hospitalized women giving birth with and without COVID-19. *JAMA Intern Med*. 2021;181(5):714–717.
9. Chinn J, et al. Characteristics and outcomes of women with COVID-19 giving birth at US academic centers during the COVID-19 Pandemic. *JAMA Netw Open*. 2021;4(8):e2120456.
10. Stock SJ, et al. SARS-CoV-2 infection and COVID-19 vaccination rates in pregnant women in Scotland. *Nat Med*. 2022;28(3):504–512.
11. Badr DA, et al. Severe acute respiratory syndrome coronavirus 2 and pregnancy outcomes according to gestational age at time of infection. *Emerg Infect Dis*. 2021;27(10):2535–2543.
12. Mor G, et al. Inflammation and pregnancy: the role of the immune system at the implantation site. *Ann N Y Acad Sci*. 2011;1221(1):80–87.
13. Abu-Raya B, et al. Maternal immunological adaptation during normal pregnancy. *Front Immunol*. 2020;11:575197.
14. Yu W, et al. Viral infections during pregnancy: the big challenge threatening maternal and fetal health. *Matern Fetal Med*. 2022;4(1):72–86.
15. Piekos SN, et al. The impact of maternal SARS-CoV-2 infection and COVID-19 vaccination on maternal-fetal outcomes. *Reprod Toxicol*. 2022;114:33–43.
16. Smith ER, et al. Adverse maternal, fetal, and newborn outcomes among pregnant women with SARS-CoV-2 infection: an individual participant data meta-analysis. *BMJ Glob Health*. 2023;8(1):e009495.
17. Wei SQ, et al. The impact of COVID-19 on pregnancy outcomes: a systematic review and meta-analysis. *CMAJ*. 2021;193(16):E540–E548.
18. DeSisto CL, et al. Risk for stillbirth among women with and without COVID-19 at delivery hospitalization - United States, March 2020-September 2021. *MMWR Morb Mortal Wkly Rep*. 2021;70(47):1640–1645.
19. Fallach N, et al. Pregnancy outcomes after SARS-CoV-2 infection by trimester: A large, population-based cohort study. *PLoS One*. 2022;17(7):e0270893.
20. Edlow AG, et al. Neurodevelopmental outcomes at 1 year in infants of mothers who tested positive for SARS-CoV-2 during pregnancy. *JAMA Netw Open*. 2022;5(6):e2215787.
21. Edlow AG, et al. Sex-specific neurodevelopmental outcomes among offspring of mothers with SARS-CoV-2 infection during pregnancy. *JAMA Netw Open*. 2023;6(3):e234415.
22. Piekos SN, et al. The effect of maternal SARS-CoV-2 infection timing on birth outcomes: a retrospective multicentre cohort study. *Lancet Digit Health*. 2022;4(2):e95–e104.
23. Simbar M, et al. Evaluation of pregnancy outcomes in mothers with COVID-19 infection: a systematic review and meta-analysis. *J Obstet Gynaecol*. 2023;43(1):2162867.
24. Vigil-Vazquez S, et al. Impact of gestational COVID-19 on neonatal outcomes: is vertical infection possible? *Pediatr Infect Dis J*. 2022;41(6):466–472.
25. Kim B, et al. Effect of severe acute respiratory syndrome coronavirus 2 infection during pregnancy in K18-hACE2 transgenic mice. *Anim Biosci*. 2023;36(1):43–52.
26. Vermillion MS, Klein SL. Pregnancy and infection: using disease pathogenesis to inform vaccine strategy. *NPJ Vaccines*. 2018;3:6.
27. Emanoil AR, et al. Focusing treatment on pregnant women With COVID disease. *Front Glob Womens Health*. 2021;2:590945.
28. Siberry GK, et al. Use of ritonavir-boosted nirmatrelvir in pregnancy. *Clin Infect Dis*. 2022;75(12):2279–2281.
29. Klein SL, et al. COVID-19 vaccine testing in pregnant females is necessary. *J Clin Invest*. 2021;131(5):e147553.
30. Lipkind HS, et al. Receipt of COVID-19 vaccine during pregnancy and preterm of small-for-gestational-age at birth — eight integrated health care organizations, United States, December 15, 2020-July 22, 2021. *MMWR Morb Mortal Wkly Rep*. 2022;71(1):26–30.
31. Watanabe A, et al. Peripartum outcomes associated with COVID-19 vaccination during pregnancy: a systematic review and meta-analysis. *JAMA Pediatr*. 2022;176(11):1098–1106.
32. Villar J, et al. Pregnancy outcomes and vaccine effectiveness during the period of omicron as the variant of concern, INTERCOVID-2022: a multinational, observational study. *Lancet*. 2023;401(10375):447–457.
33. NIH. COVID-19 Treatment Guidelines. https://www.covid19treatmentguidelines.nih.gov/therapies/antiviral-therapy/ritonavir-boosted-nirmatrelvir--paxlovid-/. Updated July 21, 2023. Accessed August 21 2023.
34. Arco-Torres A, et al. Pharmacological treatments against COVID-19 in pregnant women. *J Clin Med*. 2021;10(21):4896.
35. Burwick RM, et al. Compassionate use of remdesivir in pregnant women with severe Coronavirus Disease 2019. *Clin Infect Dis*. 2021;73(11):e3996–e4004.
36. Hsu A, et al. Ritonavir. Clinical pharmacokinetics and interactions with other anti-HIV agents. *Clin Pharmacokinet*. 1998;35(4):275–291.
37. Society for Maternal Fetal Medicine. FDA Issues EUA for the Treatment of Mild-to-Moderate COVID-19: Maternal-Fetal Medicine Subspecialists Support Use in Pregnant Patients. https://s3.amazonaws.com/cdn.smfm.org/media/3287/Treatment_1.10.pdf. Accessed July 14 2022.
38. Garneau WM, et al. Analysis of clinical outcomes of pregnant patients treated with nirmatrelvir and ritonavir for acute SARS-CoV-2 infection. *JAMA Netw Open*. 2022;5(11):e2244141.
39. Loza A, et al. Short-term pregnancy outcomes after nirmatrelvir-ritonavir treatment for mild-to-moderate coronavirus disease 2019 (COVID-19). *Obstet Gynecol*. 2022;140(3):447–449.
40. Lin CY, et al. Nirmatrelvir-ritonavir (paxlovid) for mild Coronavirus Disease 2019 (COVID-19) in pregnancy and lactation. *Obstet Gynecol*. 2023;141(5):957–960.
41. Lin K, et al. Safety and protective capability of an inactivated SARS-CoV-2 vaccine on pregnancy, lactation and the growth of offspring in hACE2 mice. *Vaccine*. 2022;40(32):4609–4616.
42. Catlin NR, et al. Reproductive and developmental safety of nirmatrelvir (PF-07321332), an oral SARS-CoV-2 M^{pro} inhibitor in animal models. *Reprod Toxicol*. 2022;108:56–61.
43. Zizioli D, et al. Developmental safety of nirmatrelvir in zebrafish (Danio rerio) embryos. *Birth Defects Res*. 2023;115(4):430–440.
44. Sones JL, Davisson RL. Preeclampsia, of mice and women. *Physiol Genomics*. 2016;48(8):565–572.
45. Leist SR, et al. A mouse-adapted SARS-CoV-2 induces acute lung injury and mortality in standard laboratory mice. *Cell*. 2020;183(4):1070–1085.
46. Hadjadj J, et al. Impaired type I interferon activity and inflammatory responses in severe COVID-19 patients. *Science*. 2020;369(6504):718–724.
47. Ogger PP, et al. Type I interferon receptor signalling deficiency results in dysregulated innate immune responses to SARS-CoV-2 in mice. *Eur J Immunol*. 2022;52(11):1768–1775.
48. Alberca RW, et al. Pregnancy, viral infection, and COVID-19. *Front Immunol*. 2020;11:1672.
49. Rad HS, et al. The effects of COVID-19 on the placenta during pregnancy. *Front Immunol*. 2021;12:743022.
50. Argueta LB, et al. Inflammatory responses in the placenta upon SARS-CoV-2 infection late in pregnancy. *iScience*. 2022;25(5):104223.
51. Huynh A, et al. SARS-CoV-2 placentitis and intraparenchymal thrombohematomas among COVID-19 infections in pregnancy. *JAMA Netw Open*. 2022;5(3):e225345.
52. Kim HM, et al. The 2009 pandemic H1N1 influenza virus is more pathogenic in pregnant mice than seasonal H1N1 influenza virus. *Viral Immunol*. 2012;25(5):402–410.
53. Chudnovets A, et al. Dose-dependent structural and immunological changes in the placenta and fetal brain in response to systemic inflammation during pregnancy. *Am J Reprod Immunol*. 2020;84(1):e13248.
54. Carpentier PA, et al. Stereotypical alterations in cortical patterning are associated with maternal illness-induced placental dysfunction. *J Neurosci*. 2013;33(43):16874–16888.
55. Littauer EQ, et al. H1N1 influenza virus infection results in adverse pregnancy outcomes by disrupting tissue-specific hormonal regulation. *PLoS Pathog*. 2017;13(11):e1006757.
56. Creisher PS, et al. Downregulation of transcriptional activity, increased inflammation, and damage in the placenta following *in utero* Zika virus infection is associated with adverse pregnancy outcomes. *Front Virol*. 2022;2:2782906.
57. Yockey LJ, et al. Type I interferons instigate fetal demise after Zika virus infection. *Sci Immunol*. 2018;3(19):eaao1680.
58. Yockey LJ, Iwasaki A. Interferons and proinflammatory cytokines in pregnancy and fetal development. *Immunity*. 2018;49(3):397–412.
59. Mayer-Barber KD, Yan B. Clash of the Cytokine Titans: counter-regulation of interleukin-1 and type I interferon-mediated inflammatory responses. *Cell Mol Immunol*. 2017;14(1):22–35.
60. Guarda G, et al. Type I interferon inhibits interleukin-1 production and inflammasome activation. *Immunity*. 2011;34(2):213–223.
61. Elovitz MA, et al. A new model for inflammation-induced preterm birth: the role of platelet-activating factor and Toll-like receptor-4.

Am J Pathol. 2003;163(5):2103–2111.
62. Hunter SK, et al. Male fetus susceptibility to maternal inflammation: C-reactive protein and brain development. *Psychol Med*. 2021;51(3):450–459.
63. Sutherland S, Brunwasser SM. Sex differences in vulnerability to prenatal stress: a review of the recent literature. *Curr Psychiatry Rep*. 2018;20(11):102.
64. Owen DR, et al. An oral SARS-CoV-2 M^{pro} inhibitor clinical candidate for the treatment of COVID-19. *Science*. 2021;374(6575):1586–1593.
65. Uraki R, et al. Characterization and antiviral susceptibility of SARS-CoV-2 Omicron BA.2. *Nature*. 2022;607(7917):119–127.
66. Nair AB, Jacob S. A simple practice guide for dose conversion between animals and human. *J Basic Clin Pharm*. 2016;7(2):27–31.
67. Costantine MM. Physiologic and pharmacokinetic changes in pregnancy. *Front Pharmacol*. 2014;5:65.
68. FDA. Fact Sheet For Healthcare Providers: Emergency Use Authorization For Paxlovid. https://www.fda.gov/media/155050/download. Updated May 2023. Accessed August 21, 2023.
69. Munoz-Fontela C, et al. Advances and gaps in SARS-CoV-2 infection models. *PLoS Pathog*. 2022;18(1):e1010161.
70. Chu H, et al. Animal models in SARS-CoV-2 research. *Nat Methods*. 2022;19(4):392–394.
71. Whipps MDM, et al. Perinatal health care access, childbirth concerns, and birthing decision-making among pregnant people in California during COVID-19. *BMC Pregnancy Childbirth*. 2021;21(1):477.
72. Lei J, et al. IL-1 receptor antagonist therapy mitigates placental dysfunction and perinatal injury following Zika virus infection. *JCI Insight*. 2019;4(7):e122678.
73. Vermillion MS, et al. Intrauterine Zika virus infection of pregnant immunocompetent mice models transplacental transmission and adverse perinatal outcomes. *Nat Commun*. 2017;8:14575.
74. Casazza RL, et al. Interferon lambda signals in maternal tissues to exert protective and pathogenic effects in a gestational stage-dependent manner. *mBio*. 2022;13(3):e0385721.
75. Engels G, et al. Pregnancy-related immune adaptation promotes the emergence of highly virulent H1N1 influenza virus strains in allogenically pregnant mice. *Cell Host Microbe*. 2017;21(3):321–333.
76. Kala S, et al. Improving the clinical relevance of a mouse pregnancy model of antiretroviral toxicity; a pharmacokinetic dosing-optimization study of current HIV antiretroviral regimens. *Antiviral Res*. 2018;159:45–54.
77. Donner B, et al. Safety of oseltamivir in pregnancy: a review of preclinical and clinical data. *Drug Saf*. 2010;33(8):631–642.
78. Watanabe S, et al. Assessing the utility of antivirals for preventing maternal-fetal transmission of zika virus in pregnant mice. *Antiviral Res*. 2019;167:104–109.
79. Sebghati M, Khalil A. Uptake of vaccination in pregnancy. *Best Pract Res Clin Obstet Gynaecol*. 2021;76:53–65.
80. Firouzbakht M, et al. Hesitancy about COVID-19 vaccination among pregnant women: a cross-sectional study based on the health belief model. *BMC Pregnancy Childbirth*. 2022;22(1):611.
81. Kourtis AP, et al. Cytomegalovirus infection in pregnancy. *Birth Defects Res*. 2014;370(23):2211–2346.
82. Neu N, et al. TORCH infections. *Clin Perinatol*. 2015;42(1):77–103.
83. Dinnon KH, et al. A mouse-adapted model of SARS-CoV-2 to test COVID-19 countermeasures. *Nature*. 2020;586(7830):560–566.
84. Creisher PS, et al. Influenza subtype-specific maternal antibodies protect offspring against infection but inhibit vaccine-induced immunity and protection in mice. *Vaccine*. 2022;40(47):6818–6829.
85. Vom Steeg LG, et al. Androgen receptor signaling in the lungs mitigates inflammation and improves the outcome of influenza in mice. *PLoS Pathog*. 2020;16(7):e1008506.
86. Vom Steeg LG, et al. Age and testosterone mediate influenza pathogenesis in male mice. *Am J Physiol Lung Cell Mol Physiol*. 2016;311(6):L1234–L1244.
87. FDA. Estimating the Maximum Safe Starting Dose in Initial Clinical Trials for Therapeutics in Adult Healthy Volunteers. https://www.fda.gov/regulatory-information/search-fda-guidance-documents/estimating-maximum-safe-starting-dose-initial-clinical-trials-therapeutics-adult-healthy-volunteers. Updated August 24, 2018. Accessed August 21, 2023.
88. Feather-Schussler DN, Ferguson TS. A battery of motor tests in a neonatal mouse model of cerebral palsy. *J Vis Exp*. 2016;(117):53569.
89. Limjunyawong N, et al. Phenotyping mouse pulmonary function in vivo with the lung diffusing capacity. *J Vis Exp*. 2015;(95):e52216.
90. Meyerholz DK, Beck AP. Histopathologic evaluation and scoring of viral lung infection. *Methods Mol Biol*. 2020;2099:205–220.
91. Meyerholz DK, et al. Approaches to evaluate lung inflammation in translational research. *Vet Pathol*. 2018;55(1):42–52.
92. Armando F, et al. SARS-CoV-2 Omicron variant causes mild pathology in the upper and lower respiratory tract of hamsters. *Nat Commun*. 2022;13(1):3519.